energies

MDPI

Article

Stability Analysis and Controller Optimization of MMC in Standalone Mode

Xingyu Liu [1], Shuguang Song [1,*], Wenzhong Ma [1] and Yusheng Wang [2]

[1] College of New Energy, China University of Petroleum (East China), Qingdao 266580, China
[2] PetroChina Planning & Engineering Institute, Beijing 100080, China
* Correspondence: shuguang.song@upc.edu.cn

Abstract: The modular multilevel converter (MMC) plays an important role in large-scale renewable energy integration and transmission, and it can also operate in standalone mode, powering AC passive loads. This paper focuses on the impact of load variation on the stability of the MMC. First, the impact of load variation on the MMC transfer function is analyzed in detail using the harmonic state-space (HSS) modeling method. Then, by means of the impedance-based stability analysis method, it is found that the MMC tends to become unstable with the increase in inductive loads. If the controller is not well-designed, the system may fail when loads change. Therefore, the worst-case design is used to guarantee the overall system's stability under all load conditions. The impact of traditional proportional resonant (PR) controller parameters on the system's stability is analyzed, revealing that the stability margin and control performance of the controller are limited. Thus, an improved controller structure with an additional series of compensators is proposed. Extensive simulation results in MATLAB/Simulink R2024a verify the analysis of this work and the effectiveness of the proposed controller.

Keywords: controller design; load variation; modular multilevel converter; stability analysis

check for updates

Citation: Liu, X.; Song, S.; Ma, W.; Wang, Y. Stability Analysis and Controller Optimization of MMC in Standalone Mode. *Energies* **2024**, *17*, 5474. https://doi.org/10.3390/en17215474

Academic Editors: Adrian Ilinca and Frede Blaabjerg

Received: 5 October 2024
Revised: 27 October 2024
Accepted: 30 October 2024
Published: 1 November 2024

Copyright: © 2024 by the authors. Licensee MDPI, Basel, Switzerland. This article is an open access article distributed under the terms and conditions of the Creative Commons Attribution (CC BY) license (https://creativecommons.org/licenses/by/4.0/).

1. Introduction

Nowadays, high-voltage direct current systems based on modular multilevel converters (MMC-HVDC) have been widely adopted owing to their advantages, such as low switching frequency, high efficiency, and high performance [1–3]. However, stability issues like wide frequency oscillation have been increasingly emerging. A number of incidents have been reported in practical MMC-HVDC projects, e.g., 20~30 Hz sub-synchronous oscillation (SSO) was reported in the Nan'ao three-terminal MMC-HVDC system in China [4] and a 1270 Hz resonance occurred in the Luxi back-to-back MMC-HVDC project [5]. Therefore, the oscillation issues in the MMC-HVDC system have received a lot of attention.

In order to analyze the oscillation phenomenon, many small-signal modeling methods have been developed, such as the dynamic phasor method [6–8], harmonic state-space (HSS) method [2,9,10], and multi-harmonic linearization method [11,12]. Guo et al. developed a comprehensive dynamic phasor-based small-signal model for MMC systems under unbalanced grid conditions, which considered the internal dynamics of the MMC system as well as the more complex controllers, and revealed the reasons for unstable oscillations [6]. Sakinci et al. developed a generalized dynamic phasor model to reduce the order of the conventional dynamic phasor model using the natural frequency separation of the variations, where the impacts of high-order harmonics on the small-signal stability of the MMC were obtained [8]. The HSS modeling approach was first introduced to characterize the multi-harmonic coupling behavior of the MMC in [2], where the accurate small-signal impedance models were developed. Wu et al. established an HSS-based MMC small-signal impedance model with the frequency-coupling dynamics considered, which was used for analyzing the SSO phenomenon [9]. Xu et al. proposed a complete HSS-based MMC small-signal impedance model considering the impedance of the grid, and the mechanism of

MMC grid impedance coupling was illustrated in detail based on the proposed model [10]. Zhu et al. presented the sequence impedance model of MMC based on the multi-harmonic linearization method and analyzed potential resonance modes, where the impact of the circulating current controller on the MMC impedance and system stability was studied [11]. In ref. [12], a special form of the multi-harmonic linearization method was adopted to reduce the complexity of the sequence impedance modeling of MMC depending on the simpler harmonic spectra.

Moreover, many oscillation suppression solutions have also been proposed to enhance the stability of the MMC, which can be divided into two categories: control parameter optimization and control structure modification. Lyu et al. analyzed the impacts of the proportional gain of the AC voltage controller on the AC-side impedance of MMC, confirming that a larger proportional gain can cause a smaller magnitude of the MMC impedance but hardly affected the resonant frequencies [2]. Huang et al. obtained the optimal controller parameters by traversing all the values within the derived boundaries of the regulator parameters, considering the delay generated by digital control [13]. Wang et al. investigated the effects of different control loop parameters on the hybrid passivity property and proposed a parameter design guideline based on the hybrid passivity criterion [14]. Moreover, many scholars also focus on the controller structure [15–21]. Wang et al. proposed a full power decoupling strategy with a new closed-loop DC-bus current proportional (P) controller for the direct-modulation-based MMC, which improved the stability of the MMC system [15]. Gao et al. presented an improved virtual impedance control method, which was the addition of the virtual resistance-inductance to ameliorate the virtual impedance control that can be equivalent to the parallel connection of resistor and inductor, and it was demonstrated that the proposed method showed better performance compared to the traditional virtual resistance control and the phase lag compensation control method [17]. Guo et al. proposed a supplementary damping controller to mitigate the low-frequency oscillations in the MMC-HVDC system under low inertia conditions by introducing a reactive power compensation signal into the reactive power outer loop control of the MMC [19]. Zhu et al. proposed a damping method with virtual arm impedance by introducing common-mode compensation terms in the insertion index to compensate for the stability defects caused by the circulating current injection methods, reducing the submodule capacitor voltage ripples [21].

Generally, MMC-HVDC systems can operate in grid-connected mode [22,23] and standalone mode [9,16]. In grid-connected mode, the MMC connects directly to a power grid, which can be either stiff or weak. In standalone mode, the MMC can connect to renewable power plants and power other different AC loads. Up to now, the grid-connected mode has been studied extensively. However, the standalone mode has not been examined in detail.

In this operation scenario, the connected loads can be modeled as resistive load R_s and inductive load L_s. Based on existing MMC stability analysis and controller design, the system can achieve stable operation under certain load conditions. However, in practical operation, the loads may vary according to the requirement, which changes the MMC operation points. When the load variation is small, the system can remain stable. However, with the increase in load variation, oscillations may appear, and in severe cases, the MMC system could even fail. How the load variation impacts the MMC internal and external small-signal characteristics still remains unknown. Therefore, it is of great importance to find out the MMC stability evolution trend to assist in designing controller structure and its parameters.

Moreover, the basic proportional resonant (PR) controller is commonly adopted for the MMC in standalone mode to achieve AC voltage control. However, the control degrees of freedom for the PR controller are limited. Given the complex harmonic interactions and small-signal dynamics of the MMC, the traditional PR controller can hardly stabilize the MMC system [9]. Additionally, the transient behavior also shows large voltage overshoot and long settling time, which is unsatisfactory. To improve the stability margin and control

performance, the existing controller structure needs to be redesigned with consideration of the MMC internal and external small-signal characteristics.

To address the above issues, in this paper, the time-domain model and frequency-domain model are first established based on the average topology of the MMC [4,10], which can effectively reflect the dynamic information of the sub-synchronous frequency range. It is worth noting that the delay generated by digital control affects the high-frequency range dynamics of the MMC. But this paper focuses on the sub-synchronous frequency range, so the delay effect is not considered. Then, the impact of load variation on the transfer function of internal small-signal perturbation to state variables is analyzed in detail using HSS. It is found that load variation significantly affects the transfer function of internal small-signal perturbation to the AC voltage perturbation response. Furthermore, the AC terminal impedance of the MMC is analyzed. It is shown that AC impedance varies along with the AC load, and the system tends to be unstable with the increase in inductive load. Therefore, the MMC controllers need to be well-designed. Otherwise, the system may fail under certain load conditions. Based on the above analysis, the worst-case design for the MMC controller considering load variation is discussed in this paper, which can ensure overall system stability. In existing literature, the proportional resonant (PR) controller is commonly used in the control loop of the MMC system [2,9,24–26]. However, given that the traditional PR controller has limited control performance and is hard to further improve the stability margin, an improved output voltage controller structure is proposed, which introduces additional series compensators according to the MMC internal small-signal dynamic nature. It is demonstrated that the proposed controller can suppress the resonant peak and decrease the phase differences up to ~110°.

The research highlights of this paper are concluded as follows:

(1) Based on the HSS method, the impact of load variation on the MMC internal (control to state variable transfer function) and external (AC terminal impedance) small-signal characteristics is studied in detail.
(2) The worst-case design for the MMC controller is adopted to ensure the overall system's stability. The control performance of the traditional PR controller is analyzed and proven to be limited.
(3) An improved output voltage controller structure with additional series compensators is proposed according to the actual MMC internal and external small-signal dynamic nature, which improves both the stability margin and control performance.

The remainder of this paper is organized as follows: Section 2 reviews the time-domain mathematical model and HSS-based small-signal model of the MMC. The impact of load variation on the MMC transfer function is examined in Section 3. Then, MMC stability is analyzed in detail in Section 4. Section 5 discusses the limitation of the PR controller and proposes the improved controller structure. Section 6 concludes this paper.

2. Modeling of Modular Multilevel Converter

In this section, the topology and mathematical model of the MMC are reviewed.

2.1. Circuit Configuration

The topology of a three-phase MMC operating in standalone mode is depicted in Figure 1. In each phase of MMC, there are two arms, namely the upper arm and the lower arm. Each arm consists of N submodules (SMs) connected in series. and are the arm inductance and resistance, respectively. The half-bridge SM structure is shown on the right-hand side, which contains a floating capacitor and two switching devices. The induction motor, which is a common industrial load, can be expressed as an inductor in series with a resistor [27]. Thus, the AC load in Figure 1 is represented by an inductor L_s connecting with the resistor R_s.

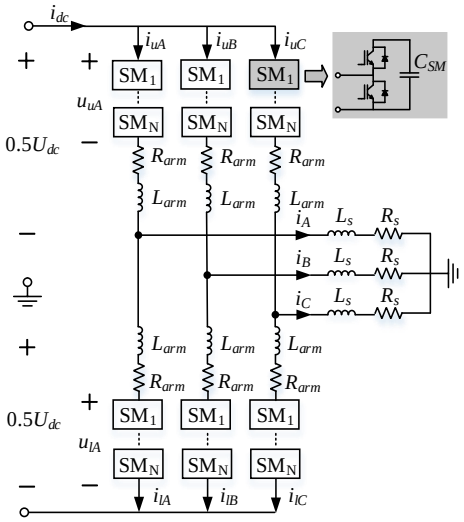


Figure 1. The topology of a three-phase MMC.

For simplification, Figure 2 gives the average model of one phase leg of the MMC, where $v_{cu\sum}$ and $v_{cl\sum}$ are the sum capacitor voltages for the upper and lower arms, respectively [28]. C_{eq} represents the arm equivalent capacitance, where $C_{eq} = C_{SM}/N$. $m_u(t)$ and $m_l(t)$ are the control signals for upper and lower arms, which can be expressed as [2]

$$\begin{cases} m_u(t) = \dfrac{1}{2}[1 - m(t) - m_2(t) + \sum_{n=3}^{\infty} m_n(t)] \\ m_l(t) = \dfrac{1}{2}[1 + m(t) - m_2(t) + \sum_{n=3}^{\infty} m_n(t)] \end{cases} \tag{1}$$

where $m(t)$ and $m_2(t)$ denote the fundamental frequency component for output control and second-order harmonic component for circulating current control, respectively. Moreover, for $n \geq 3$, $m_n(t)$ in (1) is normally equal to zero [2].

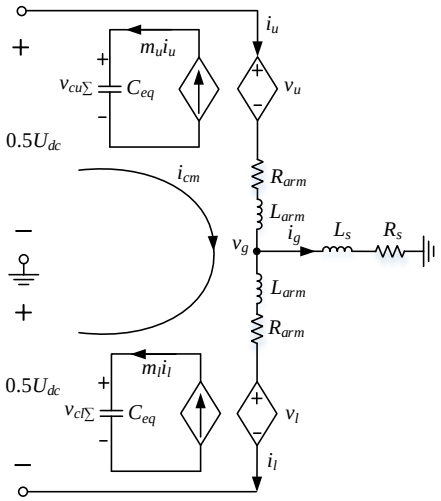


Figure 2. The average model of one phase leg of the MMC.

The circulating current $i_{cm}(t)$ and the AC output current $i_g(t)$ are defined as

$$i_{cm}(t) = \frac{i_u(t) + i_l(t)}{2} \tag{2}$$

$$i_g(t) = i_u(t) - i_l(t) \tag{3}$$

The equivalent arm output voltages can be expressed as

$$v_u(t) = m_u(t)v_{cu\sum}(t) \tag{4}$$

$$v_l(t) = m_l(t)v_{cl\sum}(t) \tag{5}$$

The capacitor charging and discharging dynamics can be expressed as [9]

$$C_{\text{eq}}\frac{dv_{cu\sum}}{dt} = m_u i_u \tag{6}$$

$$C_{eq}\frac{dv_{cl\sum}}{dt} = m_l i_l \tag{7}$$

Applying Kirchhoff's law to the upper arm and the lower arm, two circuit equations can be obtained as

$$v_u(t) + R_{arm}i_u(t) + L_{arm}\frac{di_u(t)}{dt} + v_g(t) = \frac{U_{dc}}{2} \tag{8}$$

$$v_l(t) + R_{arm}i_l(t) + L_{arm}\frac{di_l(t)}{dt} - v_g(t) = \frac{U_{dc}}{2} \tag{9}$$

where $v_g(t) = R_s i_g(t) + L_s[di_g(t)/dt]$.

Applying the differential-mode (DM) and common-mode (CM) definitions [29], the sum and difference in the control signals and equivalent SM capacitor voltages for the lower and upper arms in Figure 2 can be defined as

$$m_l(t) + m_u(t) = 2m_{cm}(t) \tag{10}$$

$$m_l(t) - m_u(t) = 2m_{dm}(t) \tag{11}$$

$$v_{cl\sum}(t) + v_{cu\sum}(t) = 2u_{Ccm}(t) \tag{12}$$

$$v_{cl\sum}(t) - v_{cu\sum}(t) = 2u_{Cdm}(t) \tag{13}$$

Substituting (1) into (10) and (11), CM and DM control signals can be written as

$$m_{cm}(t) = \frac{1}{2}[1 - m_2\cos(2\omega_1 t + \theta_{m2})] \tag{14}$$

$$m_{dm}(t) = \frac{1}{2}m\cos(\omega_1 t + \theta_{m1}) \tag{15}$$

where ω_1 represents the fundamental angular frequency.

Substituting (2)–(5) and (10)–(13) into (6)–(9), MMC dynamics in DM and CM representation are given as follows:

$$\begin{cases} \frac{di_{cm}(t)}{dt} = -\frac{R_{arm}}{L_{arm}}i_{cm}(t) - \frac{m_{cm}(t)}{L_{arm}}u_{Ccm}(t) - \frac{m_{dm}(t)}{L_{arm}}u_{Cdm}(t) + \frac{1}{2L_{arm}}U_{dc} \\ \frac{di_g(t)}{dt} = -\frac{R_{arm}+2R_s}{L_{arm}+2L_s}i_g(t) + \frac{2m_{dm}(t)}{L_{arm}+2L_s}u_{Ccm}(t) + \frac{2m_{cm}(t)}{L_{arm}+2L_s}u_{Cdm}(t) \\ \frac{du_{Ccm}(t)}{dt} = \frac{m_{cm}(t)}{\text{C}_{\text{eq}}}i_{cm}(t) - \frac{m_{dm}(t)}{2\text{C}_{\text{eq}}}i_g(t) \\ \frac{du_{Cdm}(t)}{dt} = \frac{m_{dm}(t)}{\text{C}_{\text{eq}}}i_{cm}(t) - \frac{m_{cm}(t)}{2\text{C}_{\text{eq}}}i_g(t) \end{cases} \tag{16}$$

2.2. HSS-Based MMC Steady-State Model

Based on (16), choosing the circulating current $i_{cm}(t)$, output current $i_g(t)$, CM arm capacitor voltage $u_{Ccm}(t)$, and DM arm capacitor voltage $u_{Cdm}(t)$ as state variables, the time-domain state-space model of the MMC can be expressed as

$$\dot{x}(t) = A(t)x(t) + B(t)u(t) \tag{17}$$

where

$$\dot{x}(t) = [i_{cm}(t), i_g(t), u_{Ccm}(t), u_{Cdm}(t)]^T \tag{18}$$

$$A(t) = \begin{bmatrix} -\frac{R_{arm}}{L_{arm}} & 0 & -\frac{m_{cm}(t)}{L_{arm}} & -\frac{m_{dm}(t)}{L_{arm}} \\ 0 & -\frac{R_{arm}+2R_s}{L_{arm}+2L_s} & \frac{2m_{dm}(t)}{L_{arm}+2L_s} & \frac{2m_{cm}(t)}{L_{arm}+2L_s} \\ \frac{m_{cm}(t)}{C_{eq}} & -\frac{m_{dm}(t)}{2C_{eq}} & 0 & 0 \\ \frac{m_{dm}(t)}{C_{eq}} & -\frac{m_{cm}(t)}{2C_{eq}} & 0 & 0 \end{bmatrix} \tag{19}$$

$$B(t) = diag(\frac{1}{2L_{arm}}, 0, 0, 0) \tag{20}$$

$$u(t) = [U_{dc}, 0, 0, 0]^T \tag{21}$$

The detailed HSS modeling procedure can be found in [2,9]. Thus, it is not repeated in this paper. Based on the Fourier series and harmonic balance theory, (17)–(21) can be transformed into the frequency-domain HSS model, which is expressed as

$$s\mathbf{X} = (\mathbf{A} - \mathbf{Q})\mathbf{X} + \mathbf{B}\mathbf{U} \tag{22}$$

where

$$\mathbf{X} = [X_{-h}, \ldots, X_{-1}, X_0, X_1, \ldots, X_h]^T \tag{23}$$

$$\mathbf{A} = \begin{bmatrix} A_0 & A_{-1} & \cdots & A_{-h} & & & \\ A_1 & \ddots & \ddots & \ddots & \ddots & & \\ \ddots & \ddots & A_0 & A_{-1} & \ddots & \ddots & \\ A_h & \ddots & \ddots & A_0 & A_{-1} & \ddots & A_{-h} \\ & \ddots & \ddots & A_1 & A_0 & \ddots & \vdots \\ & & \ddots & \ddots & \ddots & \ddots & A_{-1} \\ & & & A_h & \ddots & A_1 & A_0 \end{bmatrix} \tag{24}$$

$$\mathbf{B} = \begin{bmatrix} B_0 & B_{-1} & \cdots & B_{-h} & & & \\ B_1 & \ddots & \ddots & \ddots & \ddots & & \\ \ddots & \ddots & B_0 & B_{-1} & \ddots & \ddots & \\ B_h & \ddots & \ddots & B_0 & B_{-1} & \ddots & B_{-h} \\ & \ddots & \ddots & B_1 & B_0 & \ddots & \vdots \\ & & \ddots & \ddots & \ddots & \ddots & B_{-1} \\ & & & B_h & \ddots & B_1 & B_0 \end{bmatrix} \tag{25}$$

$$\mathbf{U} = [U_{-h}, \ldots, U_{-1}, U_0, U_1, \ldots, U_h]^T \tag{26}$$

$$\mathbf{Q} = diag(-jh\omega_1\mathbf{I}, \ldots, -j\omega_1\mathbf{I}, \mathbf{0}, j\omega_1\mathbf{I}, \ldots, jh\omega_1\mathbf{I}) \tag{27}$$

where **A** and **B** are called Toeplitz matrix. The subscripts h of the matrix elements represent the harmonic order. For instance, A_h, B_h are the corresponding h th Fourier coefficients of $A(t)$ and $B(t)$, respectively.

Letting the left-hand side of (22) be zero, the steady-state operation point of MMC can be calculated by

$$\mathbf{X}_{ss} = -(\mathbf{A} - \mathbf{Q})^{-1}(\mathbf{BU}) \tag{28}$$

2.3. HSS-Based MMC Small-Signal Model

To derive the small-signal model of the MMC, the harmonic linearization principle needs to be adopted. Applying the small perturbation to (17), the MMC small-signal state-space equation can be obtained as

$$x_p(t) = A(t)x_p(t) + A_p(t)x(t) + B(t)u_p(t) \tag{29}$$

where subscript p denotes the small-signal perturbation components.

In steady state, MMC contains $\pm h$ th ($h \in Z$) steady-state harmonics. According to the operation principle of the MMC, the injected small-signal perturbation with angular frequency ω_p can be coupled with these steady-state harmonics, which generates a series of harmonics with angular frequency $\omega_p \pm h\omega_1$ ($h \in Z$).

Applying the Fourier series and harmonic balance theory, (29) can be transformed into the frequency-domain model as follows:

$$s\mathbf{X}_p = (\mathbf{A} - \mathbf{Q}_p)\mathbf{X}_p + \mathbf{A}_p\mathbf{X} + \mathbf{BU}_p \tag{30}$$

$$\mathbf{X}_p = [X_{p-h}, \cdots, X_{p-1}, X_p, X_{p+1}, \cdots, X_{p+h}]^T \tag{31}$$

$$\mathbf{U}_p = [U_{p-h}, \cdots, U_{p-1}, U_p, U_{p+1}, \cdots, U_{p+h}]^T \tag{32}$$

$$\mathbf{A}_p = \begin{bmatrix} A_p & A_{p-1} & \cdots & A_{p-h} & & & \\ A_{p+1} & \ddots & \ddots & \ddots & \ddots & & \\ \ddots & \ddots & A_p & A_{p-1} & \ddots & \ddots & \\ A_{p+h} & \ddots & \ddots & A_p & A_{p-1} & \ddots & A_{p-h} \\ & \ddots & \ddots & A_{p+1} & A_p & \ddots & \vdots \\ & & \ddots & \ddots & \ddots & \ddots & A_{p-1} \\ & & & A_{p+h} & \ddots & A_{p+1} & A_p \end{bmatrix} \tag{33}$$

$$\mathbf{Q}_p = diag[j(\omega_p - h\omega_1)\mathbf{I}, \cdots, j(\omega_p - \omega_1)\mathbf{I}, j\omega_p\mathbf{I}, j(\omega_p + \omega_1)\mathbf{I}, \cdots, j(\omega_p + h\omega_1)\mathbf{I}] \tag{34}$$

However, in closed-loop control, the small-signal coefficient matrix $\mathbf{A}_p$ is related to the small-signal state variables $\mathbf{X}_p$. Therefore, (30) cannot be calculated directly, and a variable separation is needed [30], where (30) can be further reorganized as

$$s\mathbf{X}_p = (\mathbf{A} - \mathbf{Q}_p - \mathbf{G})\mathbf{X}_p + \mathbf{GR_p} + \mathbf{BU}_p \tag{35}$$

where **G** is the control matrix, which is composed of the product of the controller transfer function and steady-state state variables, and $\mathbf{R_p}$ represents the small-signal perturbation of the control reference.

Letting the left-hand side of (35) be zero, the small-signal perturbation of the state variables $\mathbf{X}_p$ can be calculated by

$$\mathbf{X}_p = -(\mathbf{A} - \mathbf{Q}_p - \mathbf{G})^{-1}(\mathbf{GR_p} + \mathbf{BU}_p) \tag{36}$$

Based on the MMC small-signal model, many scholars established the MMC terminal impedance and transfer function model to investigate the system stability and controller design issues.

3. Impact of Load Variation

In this section, the traditional controller structure is first introduced. Then, the transfer functions of internal perturbation to AC voltage and circulating current are analyzed, respectively. To support the analysis, an MMC simulation system is built in MATLAB/Simulink R2024a. The main parameters of the MMC are given in Table 1. Table 2 shows the different load conditions studied in this paper, where $|Z_s|$ remains the same but R_s/X_s varies.

Table 1. Parameters of the MMC model.

Parameters	Symbols	Values
Rated output power	P_o	100 MVA
Grid frequency	f_g	50 Hz
DC bus voltage	U_{dc}	±160 kV
AC L-L voltage (rms)	V_{grms}	166 kV
Number of the SM per arm	N	200
SM capacitance	C_{SM}	2.5 mF
Equivalent SM capacitance	C_{eq}	12.5 μF
Arm inductance	L_{arm}	0.18 mH
Arm resistance	R_{arm}	4.06 Ω

Table 2. Parameters of the AC load.

Load Conditions	R_s	L_s
Case I	275.56 Ω	0
Case II	194.85 Ω	0.6202 H
Case III	123.23 Ω	0.7845 H
Case IV	87.14 Ω	0.8321 H
Case V	54.04 Ω	0.8601 H
Case VI	45.30 Ω	0.8652 H
Case VII	34.18 Ω	0.8704 H
Case VIII	0	0.8771 H

3.1. Traditional Controller Structure

The MMC always operates in closed-loop mode rather than open-loop mode. Therefore, the traditional controller structure is introduced. In standalone mode, MMC commonly uses the voltage-controlled closed-loop form, where the AC voltage controller structure traditionally adopts the basic proportional resonant (PR) controller [2,9]. Additionally, the circulating current controller is also added in the closed-loop configuration, where the PR controller is used to suppress the second-order circulating current.

Figure 3 shows the block diagrams of the PR controllers for AC voltage and circulating current control. The delay generated by digital control affects the high-frequency range dynamics of MMC [13,31]. However, as this paper focuses on the sub-synchronous frequency range, the delay effect is not considered. The corresponding transfer functions are expressed as

$$G_{vg}(s) = K_{Pvg} + \frac{2K_{Rvg}\omega_c s}{s^2 + 2\omega_c s + \omega_1^2} \tag{37}$$

$$G_{icm}(s) = K_{Picm} + \frac{2K_{Ricm}\omega_c s}{s^2 + 2\omega_c s + (2\omega_1)^2} \tag{38}$$

where K_{Pvg}, K_{Picm}, K_{Rvg}, and K_{Ricm} are the proportional and resonant gain for the AC voltage and circulating current controller, respectively. Moreover, the resonant angular frequencies of the AC voltage and circulating current controller are tuned at ω_1 and $2\omega_1$, respectively.

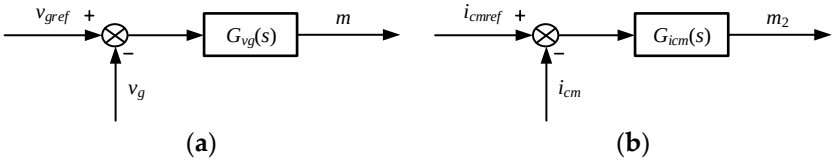


Figure 3. Block diagrams of the MMC controllers (**a**) AC voltage control; (**b**) circulating current control.

Based on the control theory, open-loop gain is crucial for analyzing the system stability, which is composed of controller and control to state variable transfer function. Therefore, in the following parts, the impact of AC load variation on the control to AC voltage and circulating current transfer functions is studied in detail.

3.2. Transfer Function of Internal Perturbation to AC Voltage

The AC voltage is controlled by the DM control signal. Thus, the internal DM small-signal perturbation $m_{dm,p}(t)$ at angular frequency ω_p with amplitude $M_{dm,p}$ in the MMC control signal should be added, which can be expressed as

$$m_{dm,p}(t) = M_{dm,p}\cos(\omega_p t) \tag{39}$$

The corresponding perturbation matrix consisting of internal DM small-signal perturbation can be expressed as $A_{dm,p}(t)$. Then, the state variable small-signal perturbation response can be expressed by

$$\mathbf{X}_p = -(\mathbf{A} - \mathbf{Q}_p)^{-1}(\mathbf{A}_{dm,p}\mathbf{X}) \tag{40}$$

By solving (40), the corresponding AC current small-signal perturbation response $i_{g,p}(t)$ can be obtained. The value of the injected internal DM small-signal perturbation to AC current transfer function at angular frequency ω_p can be calculated by

$$T_{MMC}(j\omega_p) = \frac{\mathbf{I}_{g,p}}{\mathbf{M}_{dm,p}} \tag{41}$$

where $\mathbf{I}_{g,p}$ and $\mathbf{M}_{dm,p}$ represent the phase of the AC current small-signal perturbation and the injected internal DM small-signal perturbation at angular frequency ω_p, respectively.

The value of AC voltage small-signal perturbation at angular frequency ω_p can be obtained by

$$\mathbf{U}_{g,p} = (R_s + j\omega_p L_s)\mathbf{I}_{g,p} \tag{42}$$

As a result, the value of the injected internal DM small-signal perturbation to the AC voltage transfer function at angular frequency ω_p can be calculated by

$$T_{MMC1}(j\omega_p) = \frac{(R_s + j\omega_p L_s)\mathbf{I}_{g,p}}{\mathbf{M}_{dm,p}} \tag{43}$$

And the transfer function measurement process in simulation can be described as follows: First, a DM small-signal perturbation $m_{dm,p}(t) = M_{dm,p}\cos(\omega_p t)$ is injected at angular frequency ω_p into the control signal. Then, the fast Fourier transform (FFT) module is used to obtain the magnitude and phase of the corresponding AC voltage small-signal

response at angular frequency ω_p. Change the perturbation frequency, and repeat the whole process until the measurement needs are met.

Figure 4 shows the bode diagram of the injected internal DM small-signal perturbation to AC voltage transfer functions under different AC load conditions. The solid lines and marks represent the analytical and simulated results of $T_{MMC1}(j\omega_p)$ in (43), respectively. The analytical results clearly agree well with the simulation results. It can be observed that the magnitude response is generally flat at lower frequencies. Then, a resonant peak occurs at ~28 Hz, which is augmented greatly with the increase in inductive load. The magnitude difference can reach up to 19 dB. Correspondingly, the phase response shows a significant shift around the frequency where the magnitude peaks.

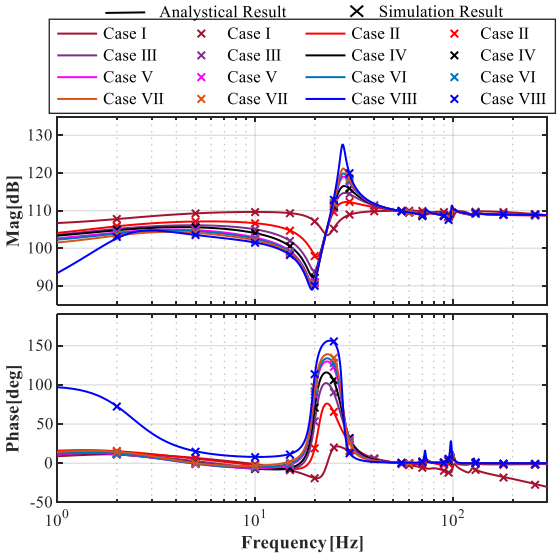


Figure 4. Model verification of internal DM perturbation to AC voltage transfer functions under different load conditions.

3.3. Transfer Function of Internal Perturbation to Circulating Current

The circulating current is controlled by the CM control signal. Therefore, a predefined internal CM small-signal perturbation $m_{cm,p}(t)$ can be injected into the control function, whose expression can be written as

$$m_{cm,p}(t) = M_{cm,p}\cos(\omega_p t) \tag{44}$$

where $M_{cm,p}$ and ω_p are the amplitude and angular frequency of internal CM small-signal perturbation, respectively. Similarly, the corresponding state variables small-signal perturbation can be calculated by

$$\mathbf{X}_p = -(\mathbf{A} - \mathbf{Q}_p)^{-1}(\mathbf{A}_{cm,p}\mathbf{X}) \tag{45}$$

Therefore, the transfer function of internal CM small-signal perturbation to circulating current at angular frequency ω_p can be calculated by

$$T_{MMC2}(j\omega_p) = \frac{\mathbf{I}_{cm,p}}{\mathbf{M}_{cm,p}} \tag{46}$$

The measurement process is similar except that an internal CM small-signal perturbation is injected in simulation. Figure 5 shows the bode diagram of the injected internal CM small-signal perturbation to circulating current transfer functions under different load conditions. The solid lines and marks are the analytical and simulation results of $T_{MMC2}(j\omega_p)$ in (46), respectively. The analytical results agree well with the simulation results as well. Compared with the AC voltage transfer function, both magnitude and phase responses

show weak correlation with different load cases. Phase differences can only be observed below 10 Hz, while there is no obvious magnitude difference, indicating that the MMC internal circulating current small-signal dynamics are hardly affected.

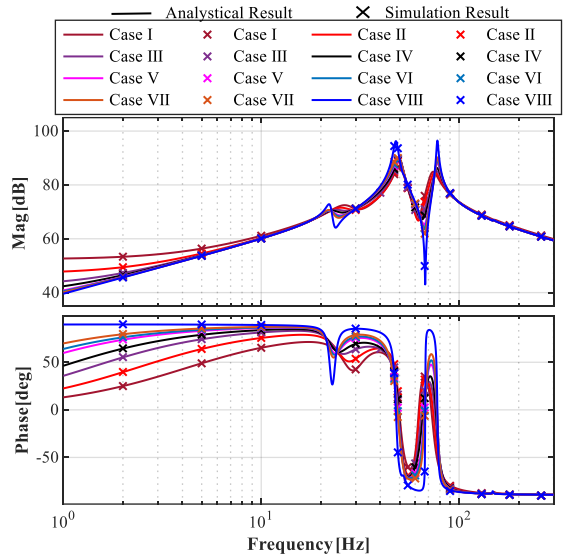


Figure 5. Model verification of internal CM perturbation to circulating current transfer functions under different load conditions.

Based on the above analysis, the load variation has a larger impact on the transfer function of internal DM small-signal perturbation to the AC voltage perturbation response. In other words, it greatly affects the stability of AC voltage control. Therefore, in the next section, a detailed discussion of the MMC stability under different load conditions is carried out.

4. MMC Stability Analysis Considering Load Variation

The analysis in the previous section verifies that load variation has a great impact on MMC small-signal dynamics. In this section, MMC stability is discussed in detail based on the impedance-based stability analysis method.

4.1. Impedance-Based Stability Analysis Method for the MMC System

To analyze the stability of closed-loop systems, the impedance-based stability analysis method is adopted. Figure 6 shows the Thevenin equivalent circuit of the MMC operating in standalone mode, where the current flowing from the MMC system to the load can be written as [32,33]

$$I(s) = \frac{v_{MMC}(s)}{Z_{Load}(s) + Z_{MMC}(s)} \tag{47}$$

which can be reorganized as

$$I(s) = \frac{v_{MMC}(s)}{Z_{Load}(s)} \cdot \frac{1}{1 + Z_{MMC}(s)/Z_{Load}(s)} \tag{48}$$

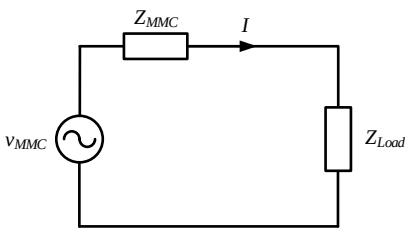


Figure 6. Thevenin equivalent circuit of MMC operating in standalone mode.

It can be assumed that the MMC voltage is stable when unloaded and the load current is stable when powered from an ideal source. Therefore, both $v_{MMC}(s)$ and $1/Z_{Load}(s)$ are stable. Then, current stability depends on (49)

$$H(s) = \frac{1}{1 + Z_{MMC}(s)/Z_{Load}(s)} \tag{49}$$

By linear control theory, $H(s)$ is stable if and only if $Z_{MMC}(s)/Z_{Load}(s)$ satisfies the Nyquist stability criterion, where the details are as follows [34]:

"If and only if the total number of counterclockwise encirclements of $(-1 + j0)$ by the eigen-loci of $Z_{MMC}(s)/Z_{Load}(s)$ is equal to the total number of right-half-plane (RHP) poles of $Z_{MMC}(s)$ and $1/Z_{Load}(s)$, the closed-loop MMC system shown in Figure 6 is stable".

Considering that $Z_{MMC}(s)$ and $1/Z_{Load}(s)$ have no RHP poles, the above criterion can be reorganized as follows:

"If and only if the eigen-loci of $Z_{MMC}(s)/Z_{Load}(s)$ does not encircle $(-1 + j0)$ counterclockwise, the closed-loop MMC system shown in Figure 6 is stable".

4.2. Stability Analysis of the Closed-Loop MMC System Under Different Load Conditions

Figure 7a shows the bode diagram of $Z_{close0}(s)$ and $Z_{Load}(s)$ of load case II with controller parameters in Table 3. The analytical results agree well with the simulation results. It is observed that the phase difference at the intersection point of $Z_{close0}(s)$ and $Z_{Load}(s)$ is much lower than 180°, which satisfies the Nyquist stability criterion. Figure 7b shows the time-domain waveforms of output voltage and current, indicating that the system works stably. Figure 7c shows the time-domain waveforms of circulating current in phase A, which fluctuates around 75 A, indicating stable system operation. And the sum capacitor voltages for the upper and lower arms remain stable, as shown in Figure 7d. It is noted that AC voltage controller parameters in Table 3 are designed based on load case II.

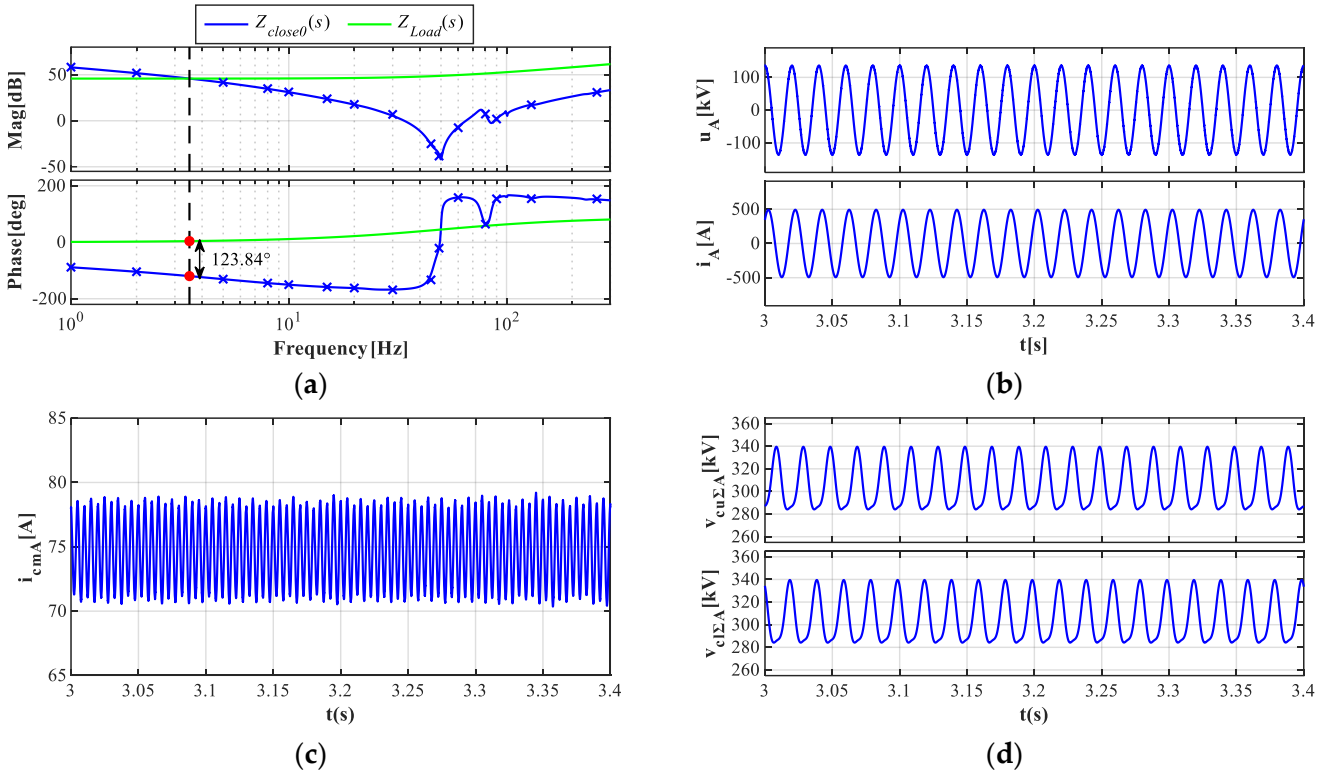


Figure 7. Bode diagrams and time-domain waveforms of load case II. (**a**) $Z_{close0}(s)$ and $Z_{Load}(s)$ (solid lines: analytical results; cross markers: simulation results); (**b**) output voltage and current; (**c**) circulating current; (**d**) sum capacitor voltages for the upper and lower arms.

Table 3. Parameters of the traditional AC voltage PR controller.

Controller Parameters	K_{Pvg}	K_{Rvg}	ω_c
Values	0.8	900	π

Figure 8a shows the bode diagram of $Z_{close0}(s)$ and $Z_{Load}(s)$ of load case VI. It can be seen that the phase difference at the intersection point is higher than 180°, which dissatisfies the Nyquist stability criterion. Figure 8b shows the corresponding time-domain waveforms of output voltage and current, where harmonic components appear. As shown in Figure 8c, the circulating current in phase A exhibits distortion. In Figure 8d, the sum capacitor voltages for the upper and lower arms contain harmonic components.

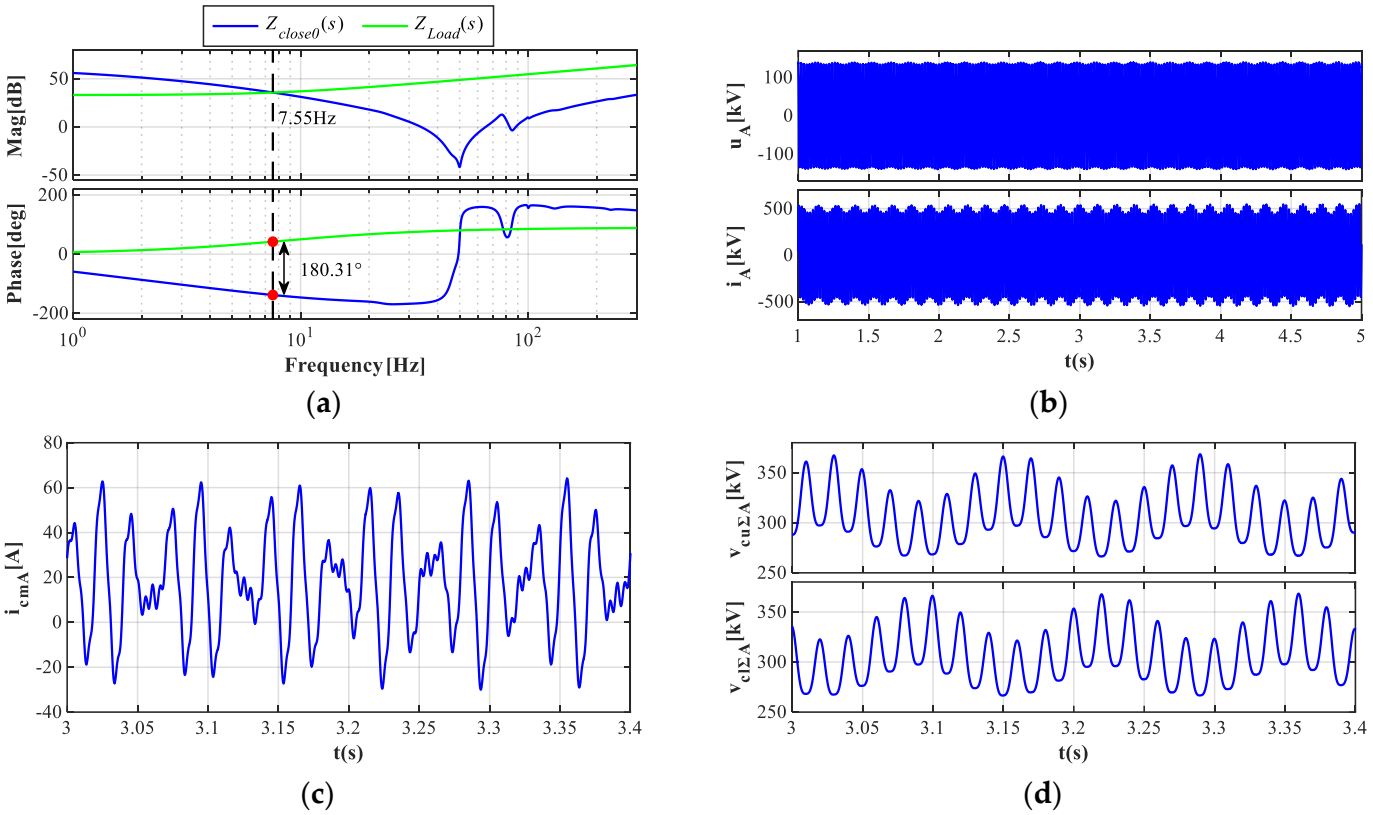


Figure 8. Bode diagrams and time-domain waveforms of load case VI. (**a**) $Z_{close0}(s)$ and $Z_{Load}(s)$; (**b**) output voltage and current; (**c**) circulating current; (**d**) sum capacitor voltages for the upper and lower arms.

Figure 9a shows the bode diagram of $Z_{close0}(s)$ and $Z_{Load}(s)$ of load case VII. It is observed that the phase difference at the intersection point is higher than 180°, which indicates the system dissatisfies the Nyquist stability criterion. Figure 9b shows the corresponding time-domain waveforms of output voltage and current, which contain large harmonic components, confirming the analysis. The corresponding circulating current contains harmonic components, as shown in Figure 9c. Similarly, in Figure 9d, harmonic components also appear in the sum capacitor voltages for the upper and lower arms. The waveforms in Figure 9c,d have already become distorted. Furthermore, time-domain waveforms of load case VIII are not shown because the system is severely unstable.

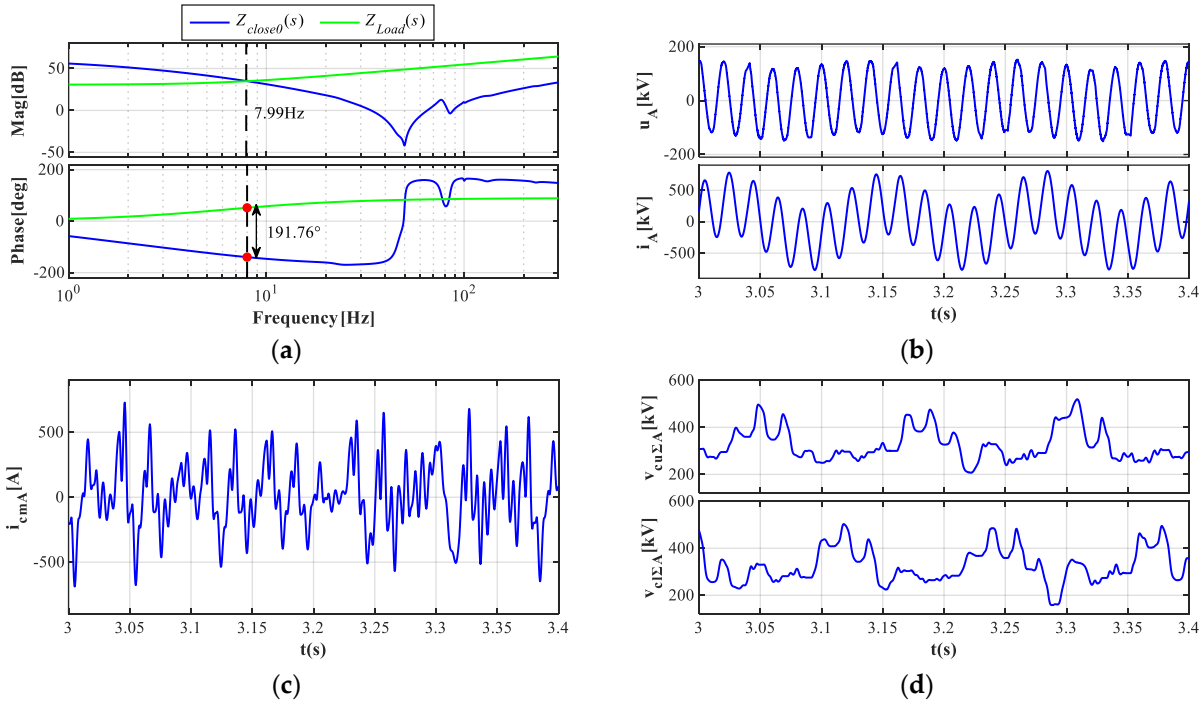


Figure 9. Bode diagrams and time-domain waveforms of load case VII. (**a**) $Z_{close0}(s)$ and $Z_{Load}(s)$; (**b**) output voltage and current; (**c**) circulating current; (**d**) sum capacitor voltages for the upper and lower arms.

Additionally, Figure 10 shows the Fourier analysis results of Figures 8b and 9b. In Figure 10a, it can be seen that SSO appears in the AC output voltage and current, where the resonant frequency is 7.5 Hz, which is close to the analytical resonant frequency of 7.55 Hz obtained in Figure 8a. In Figure 10b, SSO of 7.9 Hz appears in the AC output voltage and current. The resonant frequency of the simulation is close to the analytical resonant frequency of 7.99 Hz obtained in Figure 9a.

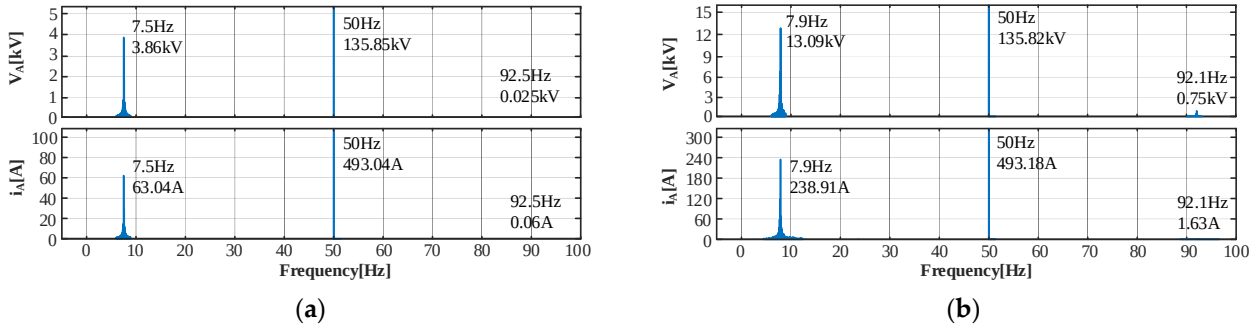


Figure 10. Fourier analysis results of load cases VI and VII. (**a**) Load case VI; (**b**) load case VII.

Based on the transfer functions shown in Figure 4 and the analysis above, the stability of the MMC with the same AC voltage controller under different load conditions is varying. The system tends to be unstable with the increase in inductive load. Thus, to guarantee the overall stability, the worst-case design is adopted for the MMC AC voltage controller design.

4.3. Verification of the Worst-Case Design

The worst load condition is case VIII. Therefore, controller parameters in Table 3 need to be adjusted according to its transfer function feature. The resonant gain K_{Rvg} is changed to 30. Figure 11 shows the bode diagrams of $Z_{close0}(s)$ and $Z_{Load}(s)$ with all load conditions. It can be seen that the phase difference at the intersection point of $Z_{close0}(s)$ and $Z_{Load}(s)$

in the worst case, VIII, is largest but lower than 180°. The phase differences are generally reduced with the decrease in inductive load, and all load conditions satisfy the Nyquist stability criterion, which ensures the overall system stability.

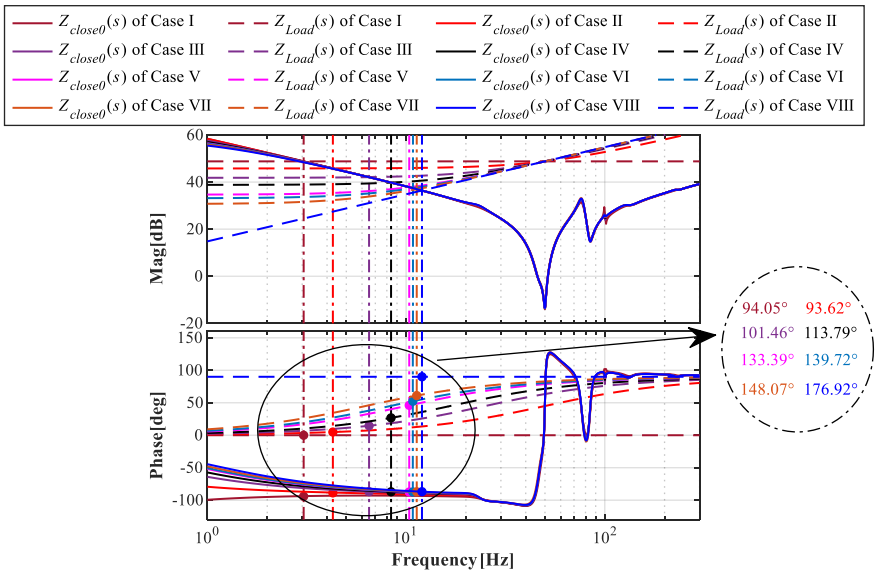


Figure 11. Bode diagrams of $Z_{close0}(s)$ and $Z_{Load}(s)$ under different load conditions.

5. Controller Optimization

5.1. Controller Parameters Optimization

By changing controller parameters, the phase differences at the intersection point of $Z_{close0}(s)$ and $Z_{Load}(s)$ vary as well. Therefore, the impact of controller parameters on system stability is studied in this part.

When K_{Rvg} is set to 30, the bode diagram of $Z_{close0}(s)$ and $Z_{Load}(s)$ of load case VIII with the tuned K_{Pvg} is shown as Figure 12a. The proportional gain K_{Pvg} = 0.8 of the AC voltage controller guarantees that the phase difference is lower than 180°. In addition, the increasing K_{Pvg} reduces the phase differences, but its influence on system stability is quite small.

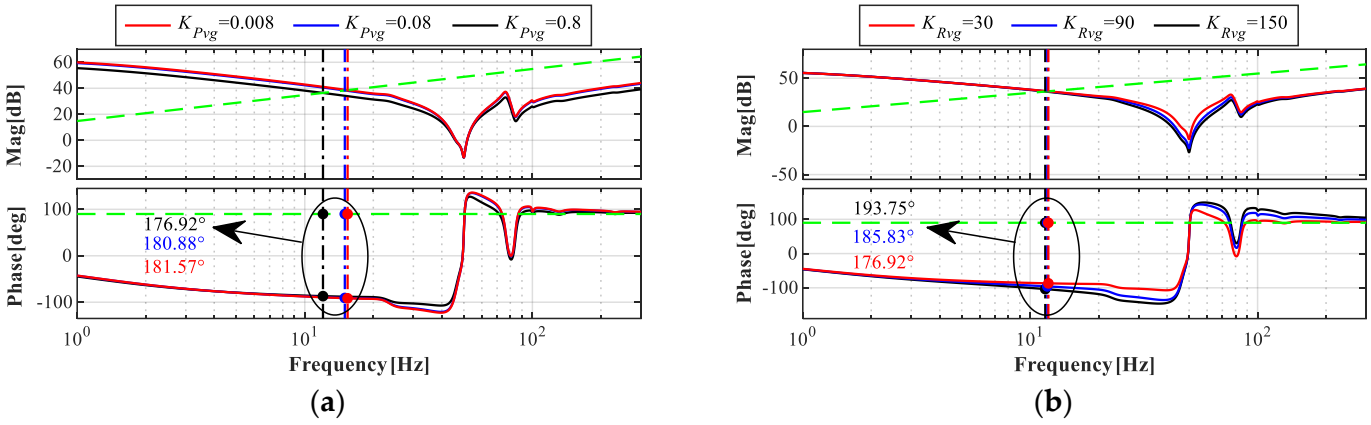


Figure 12. Bode diagrams of $Z_{close0}(s)$ and $Z_{Load}(s)$ of load case VIII with different controller parameters (Soid lines: $Z_{close0}(s)$, dashed green lines: $Z_{Load}(s)$). (**a**) Changing K_{Pvg}; (**b**) changing K_{Rvg}.

As for the resonant gain K_{Rvg}, it significantly impacts the system's stability, as shown in Figure 12b, where K_{Pvg} is set to 0.8. By tuning the resonant gain, it can be observed that the phase differences at the intersection point of $Z_{close0}(s)$ and $Z_{Load}(s)$ are gradually reduced with the decrease of K_{Rvg}. A small K_{Rvg} = 30 can ensure the system's stability.

When the resonant gains further decrease, e.g., 0.01, as shown in Figure 13a, the phase difference reduces to 172.27° but is still close to 180°. However, in this case, the AC voltage cannot track its reference value as shown in Figure 13b.

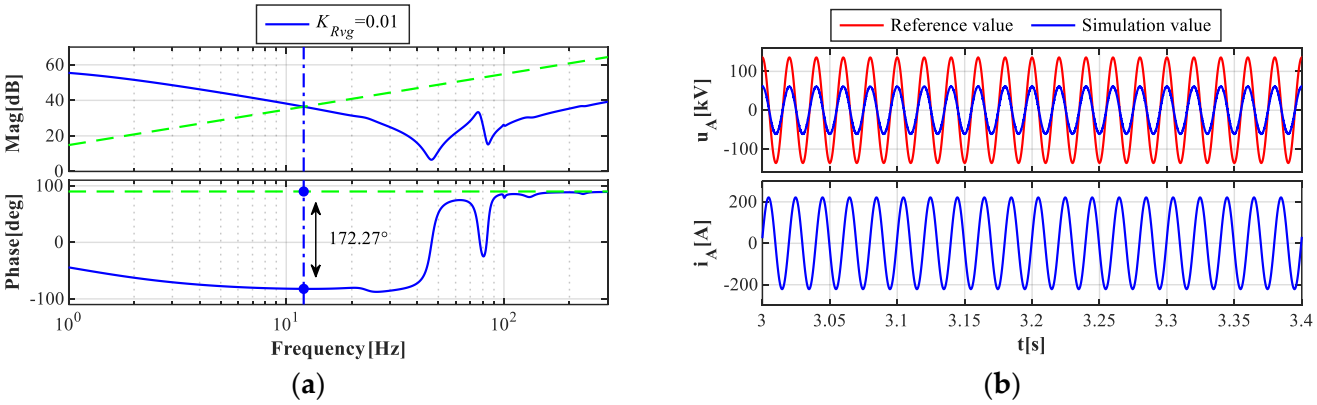


Figure 13. Bode diagrams and time-domain waveforms of load case VII (Soid lines: $Z_{close0}(s)$, dashed green lines: $Z_{Load}(s)$). (**a**) $Z_{close0}(s)$ and $Z_{Load}(s)$; (**b**) output voltage and current.

From the discussion above, it can be found that tuning the parameters of the PR controller can guarantee the system's stability. But the phase difference is relatively large and nearly impossible to further decrease. Therefore, an improved controller structure is proposed in this paper.

5.2. Proposed Controller Structure

The structure of the proposed controller is shown in Figure 14, which contains three parts:

(1) The first part is the traditional PR controller, which provides a high gain at the fundamental frequency, allowing accurate tracking of the reference signal. K_{Rvg} is the key parameter to guarantee the tracking performance.

(2) A band reject filter (BRF) is introduced, which is the second part. Based on the obtained internal DM small-signal perturbation to AC voltage transfer function, it is found that a large resonant peak appears, which affects the control performance and may threaten the system stability. The center frequency of the introduced BRF is set to suppress the resonant peak frequency at 28 Hz, and its bandwidth matches the width of the resonant peak, with a value set to 20 Hz.

(3) The third part is an additional inertia element (IE), which is added in the control loop to improve the poor stability margin of the existing PR controller. Based on the bode diagram of $Z_{close0}(s)$ and $Z_{Load}(s)$ under the worst case, the gain K_{IEvg} and cutoff angular frequency ω_{ie} of the IE are designed.

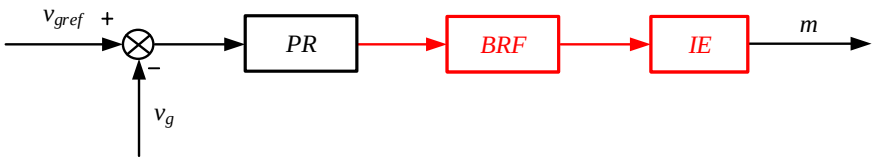


Figure 14. Block diagrams of the proposed controller structure.

The transfer function of the proposed controller can be written as

$$G_{vg}(s) = (K_{Pvg} + \frac{2K_{Rvg}\omega_c s}{s^2 + 2\omega_c s + \omega_1^2}) \cdot \frac{K_{Bvg}(s^2 + \omega_b^2)}{s^2 + 2\omega_{cb} s + \omega_b^2} \cdot \frac{K_{IEvg}}{s + \omega_{ie}} \tag{50}$$

Based on (50), the proposed controller has more control degrees of freedom, indicating that the corresponding system has better abilities in stability and control performance improvement. Figure 15 shows the flowchart of the parameter design of the proposed controller. And the corresponding parameters are given in Table 4. Figure 16 shows the bode diagram of the open-loop gain of the MMC system with the PR controller and proposed controller of the load case VIII. It can be observed that the resonant peak is suppressed, which verified the effectiveness of BRF. Moreover, the gain at the fundamental frequency remains relatively high, showing good tracking performance.

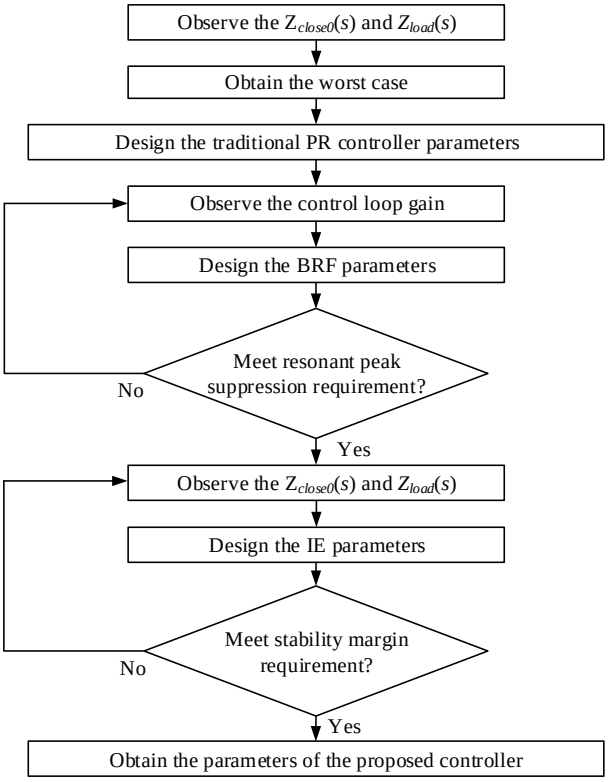


Figure 15. Flowchart of the parameter design of the proposed controller.

Table 4. Parameters of the proposed controller.

Controller Parameters	K_{Pvg}	K_{Rvg}	ω_c	K_{Bvg}	ω_b	ω_{cb}	K_{IEvg}	ω_{ie}
Values	0.8	30	π	1	56 π	40 π	200	10 π

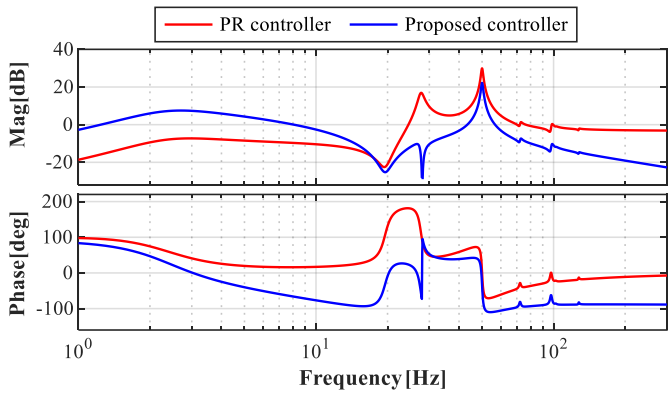


Figure 16. Bode diagram of the open-loop gain of the MMC with the traditional PR controller and the proposed controller.

Figure 17 shows the bode diagram of $Z_{close0}(s)$ and $Z_{Load}(s)$ of all load conditions with the proposed controller. It can be seen that the phase difference at the intersection point of $Z_{close0}(s)$ and $Z_{Load}(s)$ of load case VIII is equal to 114.57°. The stability margin is greatly increased, which confirms the validity and effectiveness of the proposed controller structure.

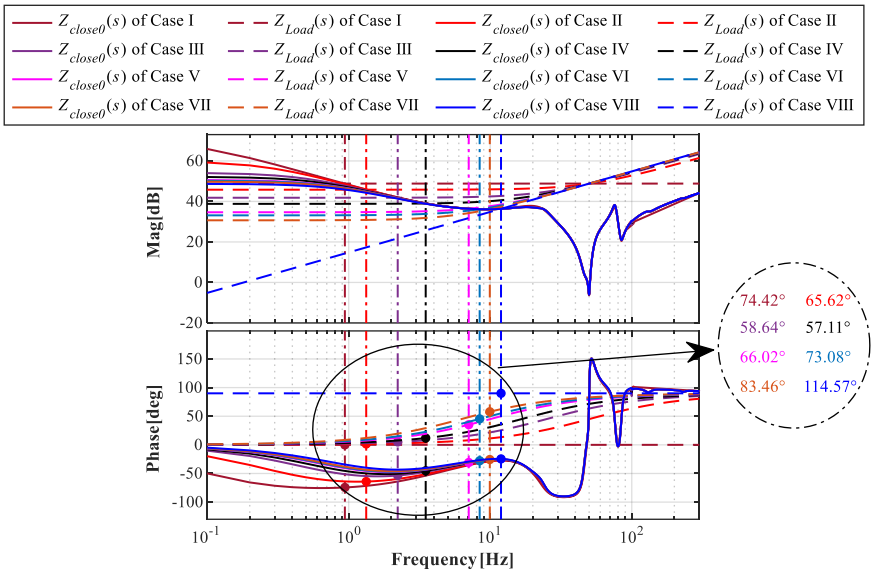


Figure 17. Bode diagrams of MMC of different load conditions with the proposed controller.

Moreover, Figure 18 shows the time-domain simulation results of the MMC with the PR controller and the proposed controller in the transient state. The AC load switches from case II to case V at t = 3.1 s. The results indicate that the MMC system reaches a stable state. However, the settling time with the proposed controller is shorter, which verifies the effectiveness of the proposed controller. The oscillation of the circulating current with the proposed controller is also smaller, as shown in Figure 18c,d. Additionally, in Figure 18e,f, the capacitor voltages also exhibit similar characteristics, further confirming the effectiveness of the proposed controller structure.

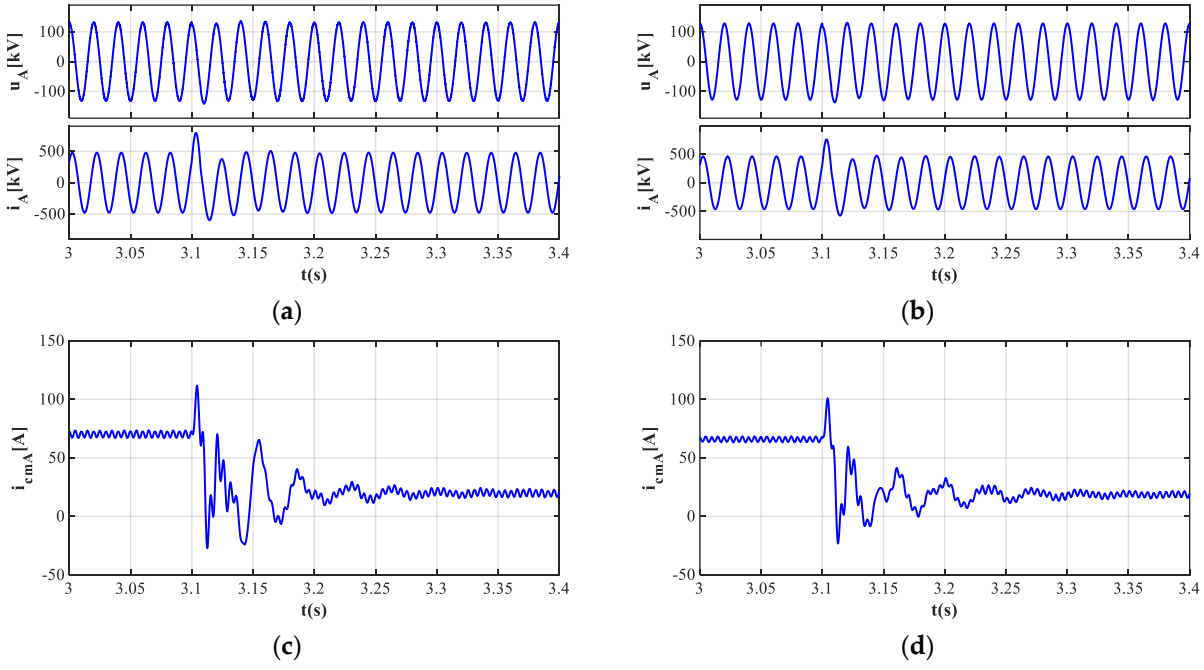
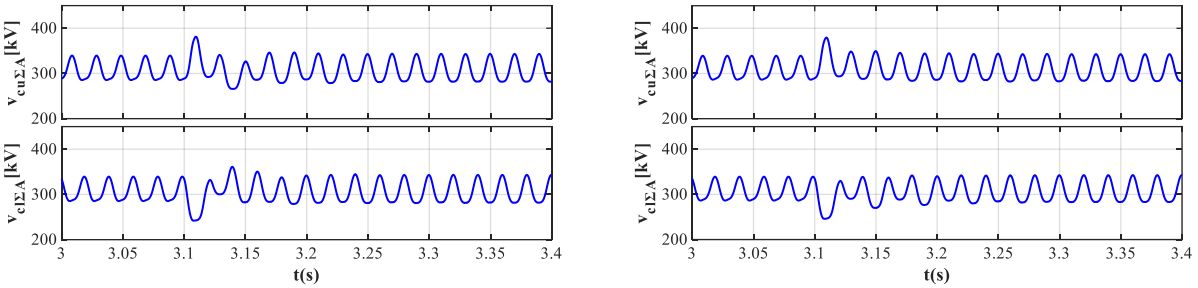


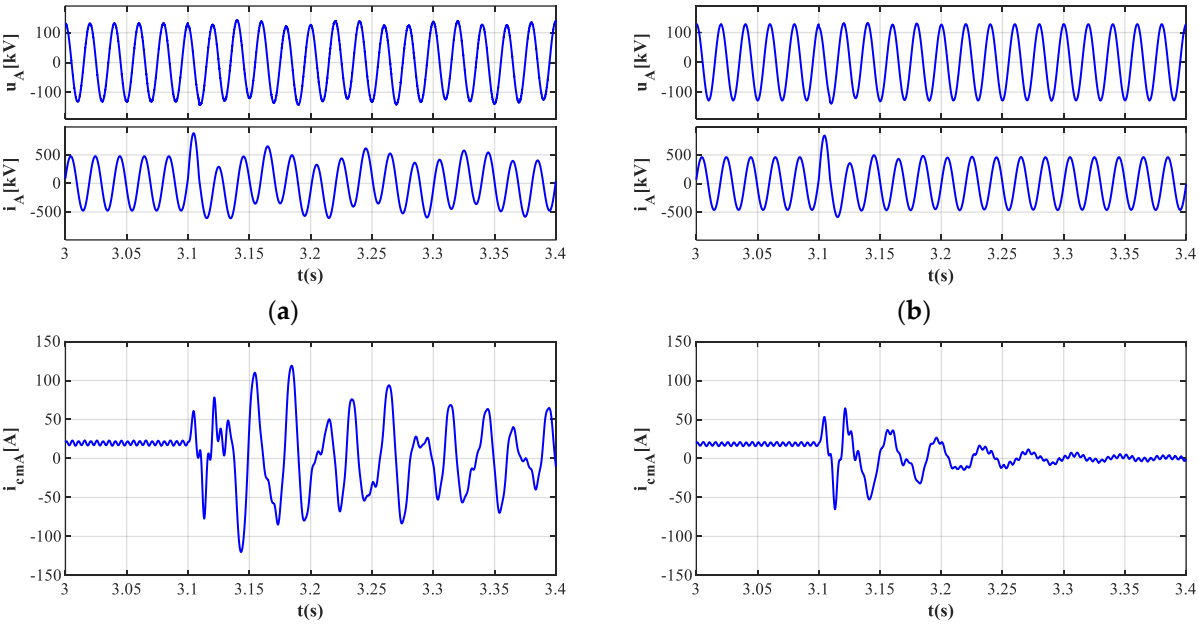
Figure 18. *Cont.*



(**e**) (**f**)

Figure 18. Transient-state time-domain waveforms from case II to case V. Output voltage and current: (**a**) traditional PR controller; (**b**) proposed controller. Circulating current: (**c**) traditional PR controller; (**d**) proposed controller. Sum capacitor voltages for the upper and lower arms: (**e**) traditional PR controller; (**f**) proposed controller.

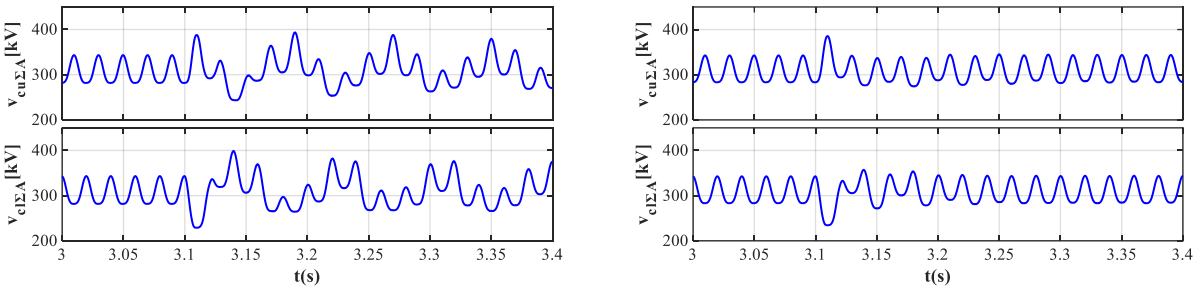
Furthermore, Figure 19 shows the corresponding time-domain simulation results, where the AC load switches from case V to case VIII at t = 3.1 s. In Figure 19a, large oscillations appear in the output voltage and current. Although the system finally reaches a stable state, the settling time is ~2.6 s, which indicates the poor control performance of the traditional PR controller. Figure 19b shows the simulation results with the proposed controller. It can be observed that the voltage and current quickly reach a stable state within only ~0.2 s, which further verifies the effectiveness of the proposed controller structure. In Figure 19c, the oscillation of the circulating current gradually decreases, with overshoot amplitude reaching ~100 A. However, for the MMC with the proposed controller, the overshoot amplitude of the circulating current is only ~50 A, as shown in Figure 19d. Additionally, Figure 19e,f indicate that the capacitor voltages have better dynamic performance with the proposed controller. In Figure 19e, the sum capacitor voltages for the upper and lower arms exhibit large overshoots, which reach ~73 kV. Figure 19f shows that the overshoot amplitudes of the sum capacitor voltages for the upper and lower arms are ~65 and ~37 kV, respectively. This further verifies the effectiveness of the proposed controller structure.



(**a**) (**b**)

(**c**) (**d**)

Figure 19. *Cont.*



(**e**) (**f**)

Figure 19. Transient-state time-domain waveforms from case V to case VIII. Output voltage and current: (**a**) traditional PR controller; (**b**) proposed controller. Circulating current: (**c**) traditional PR controller; (**d**) proposed controller. Sum capacitor voltages for the upper and lower arms: (**e**) traditional PR controller; (**f**) proposed controller.

6. Conclusions

This paper investigates the stability variation in MMC in standalone mode. Based on the HSS, the impacts of load variation on the transfer function of internal small-signal perturbation to state variables and AC terminal impedance of the MMC are analyzed in detail. It is found that the system tends to be unstable with the increase in inductive load. Therefore, a worst-case design needs to be adopted to guarantee the overall stability. Then, the impact of traditional PR controller parameters on system stability is analyzed. It is observed that the stability margin and control performance are limited. Thus, this paper proposes an improved controller structure with an additional series compensator, which can enhance the stability and suppress the resonant peak. And the transient performance is also improved. The simulation results align well with the analysis, validating the effectiveness of the proposed controller. Based on these findings, to guarantee the stability and control performance, it is recommended that a detailed small-signal analysis of all load conditions be carried out for the MMC system.

Author Contributions: Methodology, software, and writing, X.L.; formal analysis, validation, and writing, S.S.; formal analysis, investigation, W.M.; resources, funding acquisition, Y.W. All authors have read and agreed to the published version of the manuscript.

Funding: This research was funded by the Fundamental Research Funds for the Central Universities, grant number 21CX06039A.

Data Availability Statement: Data is contained within the article.

Conflicts of Interest: The authors declare no conflicts of interest.

References

1. Liu, W.; Li, K.J.; Liu, Z.; Wang, M. A Simple and Novel Precharging Control Strategy for Modular Multilevel Converter. *IEEE Access* **2019**, *7*, 170500–170512. [CrossRef]
2. Lyu, J.; Zhang, X.; Cai, X.; Molinas, M. Harmonic State-Space Based Small-Signal Impedance Modeling of a Modular Multilevel Converter with Consideration of Internal Harmonic Dynamics. *IEEE Trans. Power Electron.* **2019**, *34*, 2134–2148. [CrossRef]
3. Perez, M.A.; Ceballos, S.; Konstantinou, G.; Pou, J.; Aguilera, R.P. Modular Multilevel Converters: Recent Achievements and Challenges. *IEEE Open J. Ind. Electron. Soc.* **2021**, *2*, 224–239. [CrossRef]
4. Lyu, J.; Yin, J.; Zhu, H.; Cai, X. Impedance Modeling and Stability Analysis of Energy Controlled Modular Multilevel Converter. *IEEE Trans. Power Deliv.* **2023**, *38*, 1868–1881. [CrossRef]
5. Zou, C.; Rao, H.; Xu, S.; Li, Y.; Li, W.; Chen, J.; Zhao, X.; Yang, Y.; Lei, B. Analysis of Resonance Between a VSC-HVDC Converter and the AC Grid. *IEEE Trans. Power Electron.* **2018**, *33*, 10157–10168. [CrossRef]
6. Guo, C.; Yang, J.; Zhao, C. Investigation of Small-Signal Dynamics of Modular Multilevel Converter Under Unbalanced Grid Conditions. *IEEE Trans. Ind. Electron.* **2019**, *66*, 2269–2279. [CrossRef]
7. Zhu, S.; Liu, K.; Qin, L.; Ran, X.; Li, Y.; Huai, Q.; Liao, X.; Zhang, J. Reduced-Order Dynamic Model of Modular Multilevel Converter in Long Time Scale and Its Application in Power System Low-Frequency Oscillation Analysis. *IEEE Trans. Power Deliv.* **2019**, *34*, 2110–2122. [CrossRef]

8. Sakinci, Ö.C.; Beerten, J. Generalized Dynamic Phasor Modeling of the MMC for Small-Signal Stability Analysis. *IEEE Trans. Power Deliv.* **2019**, *34*, 991–1000. [CrossRef]
9. Wu, H.; Wang, X.; Kocewiak, Ł.H. Impedance-Based Stability Analysis of Voltage-Controlled MMCs Feeding Linear AC Systems. *IEEE J. Emerg. Sel. Top. Power Electron.* **2020**, *8*, 4060–4074. [CrossRef]
10. Xu, Z.; Li, B.; Han, L.; Hu, J.; Wang, S.; Zhang, S.; Xu, D. A Complete HSS-Based Impedance Model of MMC Considering Grid Impedance Coupling. *IEEE Trans. Power Electron.* **2020**, *35*, 12929–12948. [CrossRef]
11. Zhu, Y.; Pou, J.; Konstantinou, G. Impedance Shaping Effects of Circulating Current Controllers in Modular Multilevel Converters. In Proceedings of the 2022 International Power Electronics Conference (IPEC-Himeji 2022-ECCE Asia), Himeji, Japan, 15–19 May 2022; pp. 555–561.
12. Zhang, Y.; Chen, X.; Sun, J. Sequence Impedance Modeling and Analysis of MMC in Single-Star Configuration. *IEEE Trans. Power Electron.* **2020**, *35*, 334–346. [CrossRef]
13. Huang, T.; Yang, F.; Zhang, D.; Chen, X. High-Frequency Stability Analysis and Impedance Optimization for an MMC-HVDC Integrated System Considering Delay Effects. *IEEE J. Emerg. Sel. Top. Circuits Syst.* **2022**, *12*, 59–72. [CrossRef]
14. Wang, D.; Zhang, K. Small-Signal Stability Analysis of MMC-HVDC System Based on Hybrid Passivity. *IEEE Trans. Power Deliv.* **2024**, *39*, 29–41. [CrossRef]
15. Wang, J.; Wang, P. Decoupled Power Control for Direct-Modulation-Based Modular Multilevel Converter with Improved Stability. *IEEE Trans. Ind. Electron.* **2019**, *66*, 5264–5274. [CrossRef]
16. Xiong, X.; Yang, Y.; Wu, C.; Zhao, C.; Blaabjerg, F. Improving the Stability of Standalone MMCs by Shaping the AC Side Impedance Using Insertion Index Compensation. *IEEE J. Emerg. Sel. Top. Circuits Syst.* **2022**, *12*, 81–89. [CrossRef]
17. Gao, L.; Zhang, H.; Xu, J. An Improved Virtual Impedance Control Based Oscillation Suppression Method for MMC DC System. *CPSS Trans. Power Electron. Appl.* **2022**, *7*, 347–358. [CrossRef]
18. Huang, P.; Vanfretti, L. Multi-Tuned Narrowband Damping for Suppressing MMC High-Frequency Oscillations. *IEEE Trans. Power Deliv.* **2023**, *38*, 3804–3819. [CrossRef]
19. Guo, C.; Xu, L.; Yang, S.; Jiang, W. A Supplementary Damping Control for MMC-HVDC System to Mitigate the Low-Frequency Oscillation Under Low Inertia Condition. *IEEE Trans. Power Deliv.* **2023**, *38*, 287–298. [CrossRef]
20. Liu, W.; Wang, R.; Kerekes, T.; Dragičević, T.; Teodorescu, R. Modulation-Compensated Power Synchronization Control for Modular Multilevel Converters with Enhanced Performance Under Varying SCR. *IEEE J. Emerg. Sel. Top. Power Electron.* **2023**, *11*, 4714–4725. [CrossRef]
21. Zhu, Y.; Jiang, S.; Pou, J.; Konstantinou, G. Virtual Arm Impedance Emulation and Stability Improvement in Modular Multilevel Converters. *IEEE Trans. Power Electron.* **2024**, *39*, 3931–3942. [CrossRef]
22. Liu, Y.; Huang, M.; Tse, C.K.; Iu, H.H.C.; Yan, Z.; Zha, X. Stability and Multiconstraint Operating Region of Grid-Connected Modular Multilevel Converter Under Grid Phase Disturbance. *IEEE Trans. Power Electron.* **2021**, *36*, 12551–12564. [CrossRef]
23. Liu, Y.; Huang, M.; Zha, X.; Iu, H.H.C. Transient current estimation of MMC-HVDC systems under a grid-converter phase difference. *CSEE J. Power Energy Syst.* **2021**, *7*, 730–743.
24. Lyu, J.; Cai, X.; Molinas, M. Frequency Domain Stability Analysis of MMC-Based HVdc for Wind Farm Integration. *IEEE J. Emerg. Sel. Top. Power Electron.* **2016**, *4*, 141–151. [CrossRef]
25. Lyu, J.; Cai, X.; Molinas, M. Optimal Design of Controller Parameters for Improving the Stability of MMC-HVDC for Wind Farm Integration. *IEEE J. Emerg. Sel. Top. Power Electron.* **2018**, *6*, 40–53. [CrossRef]
26. Isik, S.; Alharbi, M.; Bhattacharya, S. An Optimized Circulating Current Control Method Based on PR and PI Controller for MMC Applications. *IEEE Trans. Ind. Appl.* **2021**, *57*, 5074–5085. [CrossRef]
27. Kundur, P. *Power System Stability and Control*; McGraw-Hill: New York, NY, USA, 1994.
28. Meng, X.; Han, J.; Pfannschmidt, J.; Wang, L.; Li, W.; Zhang, F.; Belanger, J. Combining Detailed Equivalent Model with Switching-Function-Based Average Value Model for Fast and Accurate Simulation of MMCs. *IEEE Trans. Energy Convers.* **2020**, *35*, 484–496. [CrossRef]
29. Sun, Y.; Teixeira, C.A.; Holmes, D.G.; McGrath, B.P.; Zhao, J. Low-Order Circulating Current Suppression of PWM-Based Modular Multilevel Converters Using DC-Link Voltage Compensation. *IEEE Trans. Power Electron.* **2018**, *33*, 210–225. [CrossRef]
30. Xu, Z.; Li, B.; Wang, S.; Zhang, S.; Xu, D. Generalized Single-Phase Harmonic State Space Modeling of the Modular Multilevel Converter with Zero-Sequence Voltage Compensation. *IEEE Trans. Ind. Electron.* **2019**, *66*, 6416–6426. [CrossRef]
31. Ji, K.; Chen, W.; Wu, X.; Pang, H.; Hu, J.; Liu, S.; Cheng, F.; Tang, G. High Frequency Stability Constraints Based MMC Controller Design Using NSGA-III Algorithm. *CSEE J. Power Energy Syst.* **2023**, *9*, 623–633.
32. Sun, J. Impedance-Based Stability Criterion for Grid-Connected Inverters. *IEEE Trans. Power Electron.* **2011**, *26*, 3075–3078. [CrossRef]
33. Middlebrook, R.D. Input filter considerations in design and application of switching regulators. In Proceedings of the PESC'76, IEEE Power Electronics Specialists, Conference, Cleveland, OH, USA, 8–10 June 1976; pp. 366–382.
34. Hall, S.R.; Wereley, N.M. Generalized Nyquist Stability Criterion for Linear Time Periodic Systems. In Proceedings of the 1990 American Control Conference, San Diego, CA, USA, 23–25 May 1990; pp. 1518–1525.

Disclaimer/Publisher's Note: The statements, opinions and data contained in all publications are solely those of the individual author(s) and contributor(s) and not of MDPI and/or the editor(s). MDPI and/or the editor(s) disclaim responsibility for any injury to people or property resulting from any ideas, methods, instructions or products referred to in the content.